JOURNAL OF CHEMICAL PHYSICS VOLUME 110, NUMBER 1 1 JANUARY 1999

Molecular simulation of hydrogen adsorption in single-walled carbon nanotubes and idealized carbon slit pores

Qinyu Wang and J. Karl Johnson
Department of Chemical and Petroleum Engineering, University of Pittsburgh, Pittsburgh, Pennsylvania 15261

(Received 22 July 1998; accepted 25 September 1998)

The adsorption of hydrogen gas into single-walled carbon nanotubes (SWNTs) and idealized carbon slit pores is studied by computer simulation. Hydrogen-hydrogen interactions are modeled with the Silvera-Goldman potential. The Crowell-Brown potential is used to model the hydrogen-carbon interactions. Calculations include adsorption inside the tubes, in the interstitial regions of tube arrays, and on the outside surface of isolated tubes. Quantum effects are included through implementation of the path integral formalism. Comparison with classical simulations gives an indication of the importance of quantum effects for hydrogen adsorption. Quantum effects are important even at 298 K for adsorption in tube interstices. We compare our simulations with experimental data for SWNTs, graphitic nanofibers, and activated carbon. Adsorption isotherms from simulations are in reasonable agreement with experimental data for activated carbon, but do not confirm the large uptake reported for SWNTs and nanofibers. Although the adsorption potential for hydrogen in SWNTs is enhanced relative to slit pores of the same size, our calculations show that the storage capacity of an array of tubes is less than that for idealized slit pore geometries, except at very low pressures. Ambient temperature isotherms indicate that an array of nanotubes is not a suitable sorbent material for achieving DOE targets for vehicular hydrogen storage. © *1999 American Institute of Physics.* [S0021-9606(99)70301-6]

I. INTRODUCTION

Hydrogen is a renewable and environmentally friendly energy source.[1] One of the most promising uses for hydrogen is in fuel cells for applications such as power generation and transportation. Fuel cells are electrochemical devices that convert chemical energy, provided by a fuel and oxidant, into electricity. In a typical fuel cell hydrogen and oxygen react to generate electricity, heat, and water. There are several technical challenges to the wide-spread use of hydrogen in fuel cell powered vehicles. One of the most important of these is the lack of safe and efficient hydrogen storage technologies.[1,2]

There are currently four main technologies for hydrogen storage.[3] These are: compressed gas, liquefaction, metal hydrides, and physisorption. It has been claimed that physisorption is the most promising hydrogen storage technology for meeting the goals of the DOE Hydrogen Plan for fuel cell powered vehicles.[1] The DOE Hydrogen Plan requires system weight efficiency (weight of stored H_2/system weight) of 6.5 wt % and volumetric density of 62 kg H_2 m^{-3}.[1,4] Activated carbon has been considered to be the best adsorbent for hydrogen storage.[5,8] Chahine and Bose have compared the adsorption of hydrogen on different activated carbons and zeolites.[5] It has been shown that activated carbons are better adsorbents for hydrogen than zeolites. AX-21 activated carbon shows substantially better performance than regular grade activated carbons for hydrogen storage.[5] AX-21 type carbons have cage-like pore structures. The apparent BET surface area of AX-21 carbons are on the order of 3000 m^2/g, while the surface area of regular grade microporous carbons are between 700 and 1800 m^2/g. The gravimetric density of hydrogen is about 100 g H_2/kg adsorbent and the volumetric density is around 32 kg H_2 m^{-3} in AX-21 carbons at 77 K and 50 atm. Amankwah and co-workers have measured the adsorption of hydrogen in superactivated carbon (AX-31M) at filling conditions of 150 K and 54 atm.[3] They have obtained a gravimetric density of 90 g H_2/kg adsorbent and a volume efficiency of 17.18 kg H_2 m^{-3}. While these carbons give substantially better performance than other activated carbons tested, they nevertheless do not meet the DOE targets for hydrogen storage. Hence, there is a need to develop a highly efficient adsorbent that is specifically designed for hydrogen storage. Graphitic nanofibers have very recently been proposed as a novel material for hydrogen storage.[9] These materials are claimed to have a phenomenally high capacity to adsorb hydrogen at room temperature and pressures close to 100 atm. It has been suggested that single-walled carbon nanotubes (fullerene tubes) with diameters on the order of a nanometer can adsorb large quantities of hydrogen.[4] The purpose of this paper is to evaluate the ability of single-walled carbon nanotubes (SWNTs) and idealized slit pore graphitic structures to store hydrogen under ideal conditions.

Carbon nanotubes were first produced as nested structures of concentric shells.[10] Single-wall nanotubes have subsequently been produced using catalytic metal particles in carbon-arc vaporization.[11,12] They have also been synthesized by catalytic decomposition of organic vapors[13] and laser vaporization.[14] Typical dimensions of SWNTs are 1 to 2 nm in diameter and many microns in length.[15] SWNTs selforganize into ''ropes,'' that consist of hundreds of aligned SWNTs on a two-dimensional triangular lattice, with an intertube spacing (van der Waals gap) of approximately 3.2 Å.[14,16] The van der Waals gap is defined as the distance between the walls of the nearest neighbor tubes in the bundle, as measured from the carbon centers. Nanotubes must have open ends to allow adsorption inside the tubes, but as produced, tubes are capped with hemispherical fullerene domes containing six pentagons required to produce closure. The tube ends may be opened by oxidation of the caps, which are more susceptible to oxidation because of the strained nature of the five-membered rings.[14,17,18]

SWNTs have many potential advantages for hydrogen adsorption over currently available adsorbents. They have large theoretical surface areas that are on the order of those for high-surface area activated carbons. Crystallized arrays of SWNTs have a very narrow pore size distribution that has virtually all their surface area in the micropore region. In contrast, surface area in activated carbons is broadly distributed between macropores, mesopores, and micropores. The pore sizes in an array of tubes could be controlled by tuning the diameter of the SWNTs making up the array. Theoretical calculations predict that carbon nanotubes have very strong capillary forces for encapsulating both polar and nonpolar fluids.[19,20] The filling of multiwalled nanotubes with liquid lead has been experimentally observed.[21] Wet chemistry techniques have recently been used to open SWNTs and form single crystals of ruthenium metal inside the nanotubes.[22] Dillon and co-workers have used temperature programmed desorption to study hydrogen adsorption on carbon soots containing small amounts of SWNTs.[4] They reported high hydrogen uptake under conditions that do not induce adsorption on activated carbon or carbon soots that do not contain nanotubes. Maddox and Gubbins have modeled adsorption of argon and nitrogen in single- and double-walled nanotubes.[23] They found that argon and nitrogen are strongly adsorbed in a SWNT of diameter 1.02 nm. Layering transitions and hysteresis were observed for double-walled nanotubes with a diameter of 4.78 nm. Model calculations for the adsorption of hydrogen in a SWNT at low coverage (zero pressure limit) were performed by Stan and Cole.[24] The quantum motion of hydrogen molecules was treated by the effective potential method. The effects of the corrugation of the solid potential were included by treating the carbon atoms in the nanotube explicitly.

We present calculations of hydrogen adsorption in arrays of SWNTs and isolated SWNTs at 77, 133, and 298 K over a range of pressures. Simulations at 133 K were performed to facilitate comparison with the experiments of Dillon *et al.*[4] In order to compare SWNTs with activated carbon and graphitic nanofibers on an equal theoretical footing, we perform simulations of hydrogen adsorption in idealized graphitic slit pores. The pore width is chosen to maximize the adsorptive capacity of slit pores. This model has previously been used to estimate the maximum adsorptive capacity of activated carbon for methane.[25,26] Graphitic slit pores are used as a first approximation to the structure of graphitic nanofibers, recently used as sorbents for hydrogen storage.[9]

TABLE I. Potential parameters for the Crowell-Brown potential.

Parameter	Value	Parameter	Value
$P_\parallel$	0.57 Å^3	$P_\perp$	1.995 Å^3
P_H	0.81 Å^3	ρ	0.382 Å^{-2}
E_H	2.337×10^5 K	E_C	1.39254×10^5 K
σ_CC	3.43 Å	σ_HH	3.075 Å

II. POTENTIAL MODELS

Hydrogen molecules are treated as structureless spherical particles. This has been found to be a good approximation for fluid and solid hydrogen at reasonable pressures.[27–31] The H_2-H_2 interaction is modeled by the Silvera-Goldman potential,[31] which is a pair potential that includes a pair-wise effective three-body term.

Idealized carbon slit pores are modeled by single graphite sheets with a pore width H. The pore width H is defined as the distance between graphite sheets, as measured from the carbon centers. We use the Crowell-Brown potential[32] to model the interaction between H_2 and the graphite sheets. Crowell and Brown derived a laterally averaged interaction potential for H_2 on the basal plane of graphite.[32] We chose the Crowell-Brown potential because the anisotropy of the polarizability of graphite is explicitly taken into account. The Crowell-Brown potential, summed over $n+1$ graphite sheets parallel to the surface, is given by

$$V_{sf}(z)=\frac{-\pi\rho E_\mathrm{H}E_\mathrm{C}P_\mathrm{H}P_\parallel}{(E_\mathrm{H}+E_\mathrm{C})h_0^4}\times\left[\frac{3}{8}\left(1+\frac{P_\perp}{P_\parallel}\right)\sum_{i=0}^{n}(x+i)^{-4}-\frac{\sigma_\mathrm{CH}^6}{5x^{10}h_0^6}\left(1+\frac{P_\perp}{2P_\parallel}\right)\right], \tag{1}$$

where E_H and E_C are atomic energies for hydrogen and carbon, respectively, $P_\parallel$ and $P_\perp$ are atomic polarizabilities, where the subscripts denote orientations parallel to and perpendicular to the graphite c axis, P_H is the polarizability of hydrogen, ρ is the carbon atom planar density, h_0 is the interlayer spacing of graphite, and $x=z/h_0$. In our case we set h_0 equal to the pore width H. The values of the parameters are given in Table I. We truncated the sum after $n=5$. The error due to truncating the sum is less than 1 K (0.1%) at the minimum of the potential well. We have performed additional simulations with $n=10$ to evaluate the effect of the truncation. The error caused by the truncation of the potential after $n=5$ is generally very small, especially at high pressures. The solid-fluid interaction experienced by a hydrogen molecule at a position z in a carbon slit pore of width H is the sum of the interactions with graphite planes above and beneath,

$$V_{sf}(z,H)=V_{sf}(z)+V_{sf}(H-z). \tag{2}$$

The hydrogen-nanotube interaction is modeled by the Crowell-Brown potential for hydrogen interacting with carbon atoms in an oriented graphitic sheet. The hydrogen-carbon potential is given by

$$V(r_i,\phi_i)=\frac{E_{\mathrm{H}}E_{\mathrm{C}}P_{\mathrm{H}}P_{\parallel}(1+P_{\perp}/2P_{\parallel})\sigma_{\mathrm{CH}}^{6}}{(E_{\mathrm{C}}+E_{\mathrm{H}})r_i^{12}}-\frac{E_{\mathrm{H}}E_{\mathrm{C}}P_{\mathrm{H}}[3(P_{\parallel}-P_{\perp})\cos^2\phi_i+(P_{\parallel}+5P_{\perp})]}{4(E_{\mathrm{H}}+E_{\mathrm{C}})r_i^{6}},\tag{3}$$

where r_i is the distance from carbon atom i in the tube, to the hydrogen molecule (which could be either inside or outside the tube), and ϕ_i is the angle between the axis normal to the tube surface and a line connecting the hydrogen and carbon atoms. The anisotropy of the polarizability of the graphite sheet making up the tube is taken into account through this potential. It is important to note that no account is made for the perturbation of the potential due to curvature induced strain of the carbon sp^2 bonding network, or due to the electronic properties of the tube, which depend on chirality.[33–35] We assume that the positions of the individual carbon atoms in the tube are unimportant at the temperatures of interest in this study. At very low temperatures corrugation effects would become important. An effective potential is developed by integrating over the positions of all carbon atoms in a unit cell of the tube. The potential for a hydrogen molecule inside a nanotube is denoted $V(r,z,\theta)$, where r is the distance from the center of the tube, z is the distance along the tube axis, and θ is the radial angle. This can be reduced to a one-dimensional potential by integrating over z and θ for each value of r. We have applied a cutoff distance of 30 Å for the H_2-C interactions by including several unit cells of the tube. The averaged fluid-wall potential inside the tube is given by

$$V(r)=\frac{1}{2\pi L_{\mathrm{cell}}}\int_0^{L_{\mathrm{cell}}}\int_0^{2\pi}V(r,\theta,z)\,d\theta\,dz,\tag{4}$$

where L_{cell} is the length of a unit cell of the tube. We note that an analytic expression for the solid-fluid potential inside a cylindrical pore has been developed by Tjatjopoulos *et al.*[36] for spherical Lennard-Jones interactions. Romberg quadrature[37] was used to numerically integrate over θ and z. The averaged potential was fitted to a seventh-order polynomial,

$$V(r)=\sum_{i=0}^{7}a_i\left(\frac{R}{R-r}\right)^i,\tag{5}$$

where R is the radius of the tube. The interaction potential for hydrogen with the external surface of an isolated tube was computed in a similar fashion. The solid-fluid potential for an array of tubes includes the interaction of hydrogen with all the carbon atoms within the cutoff distance in the tube array. We have performed simulations for two different achiral nanotubes, denoted as (9,9) and (18,18) in the notation of Hamada *et al.*[34] The (9,9) tube has a diameter of about 12.2 Å and the (18,18) tube has a diameter of 24.4 Å. Figure 1 shows the solid-fluid potentials for the idealized slit pore, the (9,9), and the (18,18) tube arrays. The potentials for the (9,9) and (18,18) isolated tubes are not shown. The depth of the potential well for the (9,9) tube array is larger than that for the slit pore with a width of $H^*=3$ because the curvature of the tube increases the number of nearest neighbor carbon atoms. The potential curve for the isolated (9,9) tube has the same shape as that for the (9,9) tube array, but the well depth of the tube array is 55 K deeper. The isolated (18,18) tube potential is almost identical to the potential for the (18,18) tube array.

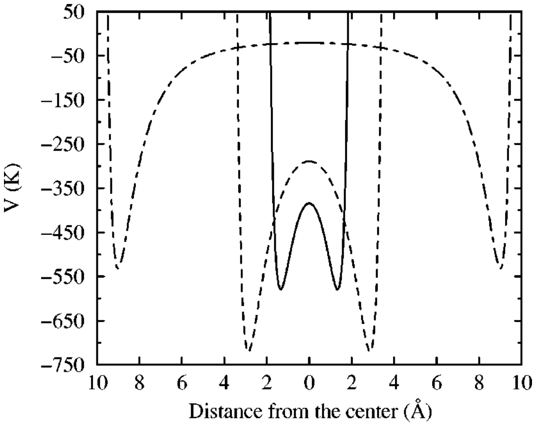

FIG. 1. Adsorption potentials for hydrogen in tube arrays and idealized slit pores. The solid line denotes the idealized carbon slit pore with a pore width of $H^*=3$. The dashed line is the potential for a (9,9) tube array, and the dot-dashed line represents a (18,18) tube array.

In our simulations we account for the adsorption of hydrogen in the interstitial regions (where three tubes meet) of a tube array. The fluid-wall potential of a hydrogen molecule located in the interstice was calculated by summing over the interactions of an adsorbate molecule and three nearest tubes,

$$V(r,\theta)=V(r_1)+V(r_2)+V(r_3),\tag{6}$$

where r_1, r_2, and r_3 are the distances from the hydrogen molecule to the centers of the three nearest tubes, and $V(r)$ is the averaged potential for a hydrogen molecule outside a nanotube. $V(r)$ was computed with the same method as that for the potential inside a nanotube. Unlike the potential inside the tube, the fluid-wall potential in the interstice is not cylindrically symmetric.

III. SIMULATION METHOD

The path integral method of Feynman[38] has been used to account for the quantum effects of hydrogen. In the path integral formalism, each quantum particle is replaced by a classical ring polymer. The number of beads on the polymer is increased until no further changes in the equilibrium properties of the ring polymer system are noted. The proper statistical mechanical averages of the classical ring polymer system yield the equilibrium properties of the quantum system of interest. We have combined multiple-time step path integral hybrid Monte Carlo with grand canonical Monte Carlo (GCMC), giving a direct method for computing the adsorption of quantum fluids.[30] A detailed discussion of this method can be found elsewhere.[29,30] Three types of moves are involved in the GCMC method: (i) displacement, (ii) creation, and (iii) deletion. Molecule displacements are accomplished with the multiple-time step path integral hybrid Monte Carlo algorithm.[39] In the molecule creation step, a path is inserted in the simulation box with a random position

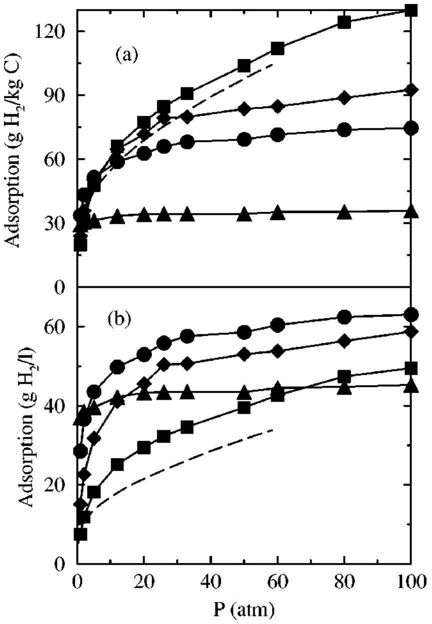

FIG. 2. Adsorption isotherms for hydrogen in idealized carbon slit pores of various widths at 77 K. Triangles are for the $H^*=2$ pore, circles are for $H^*=3$, diamonds are for $H^*=4$, and squares are for $H^*=6.67$. The dashed lines represent experimental data for AX-21 from Ref. 6. The gravimetric densities are given in (a) and the volumetric densities are shown in (b).

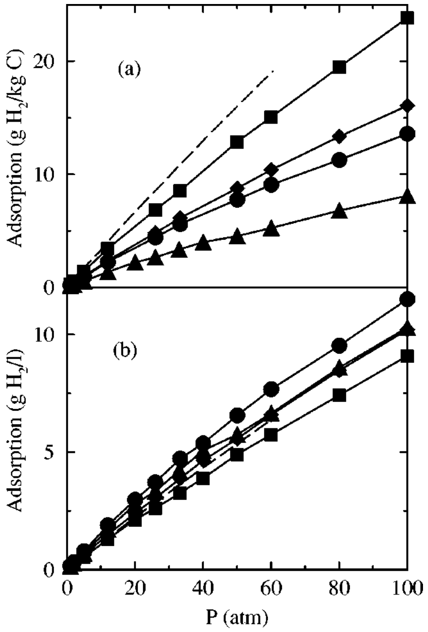

FIG. 3. Adsorption isotherms for hydrogen in idealized carbon slit pores of various widths at 298 K. Triangles are for the $H^*=2$ pore, circles are for $H^*=3$, diamonds are for $H^*=4$, and squares are for $H^*=6.67$. The dashed lines represent experimental data for AX-21 from Ref. 7. The gravimetric densities are given in (a) and the volumetric densities are shown in (b).

and random orientation. The conformation is picked randomly from the conformations of a system of ideal gas ring polymers. The probabilities of making a displacement, a molecule creation, and a deletion were set to 0.1, 0.45, 0.45, respectively. The bead-bead intermolecular cutoff was set to $5\sigma_{ff}$, where the σ_{ff} is the diameter of the fluid molecules. No long range corrections was applied. Classical simulations for hydrogen were also carried out to assess the importance of quantum effects. The classical simulations used exactly the same fluid-fluid and solid-fluid potentials as the path integral simulations; the only difference being that the number of beads per ring was always set to unity in the classical calculations.

Adsorption isotherms of hydrogen in idealized carbon slit pores with reduced pore widths $H^*=H/\sigma_{ff}$ of 2, 3, 4, and 6.7 have been computed at temperatures of 77 and 298 K. The number of beads per ring was set to 15 at 77 K, and 5 at 298 K. Periodic boundary conditions in x and y directions were employed. The lateral dimensions of the box, $L_x=L_y$, were chosen to be 10–30σ_{ff}, which gave average numbers of molecules ranging from 80 to 200.

We have calculated the adsorption of hydrogen on the internal and external surfaces of an isolated tube. By isolated tubes, we mean tubes that are far enough apart from each other that the interactions between adsorbate molecules on different tubes in the array are negligible. The simulations were carried out in a rectangular box, with the tube in the center. Periodic boundary conditions were employed in all three directions. The lateral dimensions of the box, $L_x=L_y$ were chosen to be $10\sigma_{ff}$ and $14\sigma_{ff}$ for the (9,9) and (18,18) tubes, respectively. The lateral box dimensions were chosen so that the distance between adjacent tubes was larger than $6\sigma_{ff}$, which allowed the interaction of adsorbate molecules with neighboring tubes to be neglected. The height of the simulation box was 10–20σ_{ff}, which gave average numbers of molecules ranging from 50 to 300, depending on the state point. Molecules were inserted inside or outside the tube with equal probabilities.

Path integral simulations of hydrogen in an array of tubes are extremely CPU intensive because of the number of solid-fluid and fluid-fluid interactions to compute when neighboring tubes are included. As a reasonable first approximation to adsorption in a full array of tubes we have computed adsorption in a single tube with the effective potential for a tube array. The height of the tube was chosen to be 20–40σ_{ff}. The average number of molecules ranged from 50 to 200. Periodic boundary conditions were applied only in the z direction. Adsorption in the interstice was evaluated through separate GCMC simulations of a single interstice bounded by three tubes.

IV. RESULTS AND DISCUSSIONS

A. Adsorption in carbon slit pores

We have calculated the adsorption isotherms for the idealized slit pores of three widths, $H^*=2$ (6 Å), 3 (9 Å), 4 (12 Å), and 6.7 (20 Å). These widths correspond to being able to hold a maximum of one, two, three, and five layers of adsorbed hydrogen, respectively. Simulations were performed at 77 and 298 K over a pressure range of 1 to 100 atm. Adsorption isotherms are shown in Figs. 2 and 3. We show the total gravimetric (g H_2/kg C) and volumetric (g H_2/ℓ) densities, because both are important criteria for evaluating hydrogen storage systems. The theoretical surface area of idealized carbon slit pores is 2620 $m^2\ g^{-1}$.

The smallest slit pore ($H^*=2$) has the highest uptake at the very lowest pressures because it exhibits the strongest solid-fluid interaction potential. However, at higher pressures wider pores have a higher storage capacity because the $H^*=2$ pore can only hold a single layer of hydrogen. At 77 K the total amount of hydrogen adsorbed in the $H^*=2$ pore remains essentially constant over the entire pressure range (see Fig. 2). The density of hydrogen inside the $H^*=2$ pore quickly reaches a value of 0.3 $\mathrm{cm}^3/\mathrm{m}^2$, which is close to the experimentally observed monolayer coverage 0.32–0.35 $\mathrm{cm}^3/\mathrm{m}^2$,[40–42] even though the temperature is over twice the critical temperature of hydrogen. In contrast, the two largest pores do not completely fill even for a pressure of 100 atm.

From Fig. 2(a) it is clear that the optimum pore size for hydrogen storage depends upon the storage pressure. At low pressures, the pore with a width of $H^*=3$ holds the most hydrogen on a per weight basis, but at pressures greater than about 5 atm the larger pores are more effective. This is because the weight fraction is dominated by the amount of available pore space at higher pressures. The volumetric density is shown in Fig. 2(b). The smallest pore gives the highest volumetric density at pressures lower than 1.5 atm, while the $H^*=3$ pore holds the most hydrogen per unit volume over a wide range of pressures. This is in agreement with the simulation results of Matranga *et al.*[25] and Cracknell *et al.*[26] for methane storage. Experimental data for adsorption on activated carbon (AX-21) from Bénard and Chahine[6] are plotted in Fig. 2 along with the simulation data. Simulations for the $H^*=6.7$ slit pore agree quite well with the activated carbon data on a per weight basis. The agreement is rather fortuitous, considering the simplicity of the model adsorbent compared with AX-21. The volumetric density of adsorbed hydrogen on AX-21 is much lower than any of the idealized slit pores, reflecting the low density of the activated carbon (0.3 $\mathrm{g\ cm}^{-3}$).

Hydrogen adsorption at 298 K in slit pores from simulations is shown in Fig. 3, along with experimental data[7] for adsorption on AX-21. The storage capacity is much lower at 298 K than at 77 K. The amount of adsorption is roughly lowered by a factor of 6 for the pore of width $H^*=3$. In contrast to adsorption at 77 K, the smallest pore is not completely filled even up to 100 atm. This indicates that the density of hydrogen is not liquid-like inside the $H^*=2$ pore, even at the highest pressures studied. The gravimetric density increases with the pore width, as the pore volume tends to be more important than the solid-fluid interaction potential at this high temperature. The pore with a width of $H^*=3$ gives the highest volumetric density over the entire pressure range.

We now compare the idealized slit pore of width $H^*=3$ with the AX-21 activated carbon. The $H^*=3$ slit pore has a bulk density of 0.85 $\mathrm{g\ cm}^{-3}$, while AX-21 has a bulk density of 0.3 $\mathrm{g\ cm}^{-3}$.[5,7] At 77 K, the volumetric densities in the slit pore are 100%, 150%, 200%, and 250% higher than those in AX-21 at 50, 20, 5, and 1 atm, respectively. The gravimetric densities in the $H^*=3$ pore are higher than in AX-21 at pressures below 13 atm at 77 K. However, the pore holds less hydrogen per weight of carbon at higher pressures because of the larger pore volumes available in AX-21. At 298 K AX-21 gives slightly higher volumetric densities than the slit pore at pressures less than 15 atm. This may be due to high-energy sites present on activated carbon that are not accounted for in our slit pore model. These sites may be due to either chemical heterogeneity or to geometric features such as corner sites.[43,44] For higher pressures the slit pore holds approximately 10% more hydrogen on a volumetric basis than AX-21. The total gravimetric density at 298 K is somewhat higher for AX-21 than for any of the idealized slit pores. The higher gravimetric density for AX-21 reflects the larger pores available relative to the idealized slit pores. The excess gravimetric densities from simulations and experiments at 298 K (not shown) are in closer agreement than the total densities, but the simulations are still systematically lower than the experimental data for AX-21. This indicates that the higher gravimetric density for AX-21 cannot be completely explained by the larger pores.

The simulation results for idealized slit pores at 298 K and a pressure of 100 atm can be compared with the experimental data for hydrogen adsorption on graphitic nanofibers at about the same conditions.[9] The graphite nanofibers consist of parallel stacks of graphite platelets, 30–500 Å in width, and having lengths of tens to hundreds of microns.[9] This configuration suggests that our model of idealized slit pores would be an appropriate first-order approximation to this structure, although all edge effects are ignored in our calculations. The experiments were performed by charging a vessel containing a small amount of carbon nanofiber sorbent with hydrogen at 298 K and pressures around 100 atm. The pressure drop was monitored as a function of time. The system was assumed to be in equilibrium after the pressure stabilized. The process took on the order of 24 h, and the difference between the initial and final pressures was used to compute the amount of hydrogen adsorbed (excess adsorption) on the nanofibers. In order to model this system we compare the gravimetric densities from the 298 K isotherms at a pressure of 100 atm for each of the slit pores. This does not correspond exactly to the experimental setup, but it is easy to see that the simulation method will overestimate the amount of hydrogen adsorbed compared with the experimental situation where the pressure is allowed to drop during adsorption. Experimental measurement of the spacing between the graphite platelets gives a value of 3.4 Å, similar to the spacing between layers of turbostratic graphite. We note that it is not possible for hydrogen to adsorb into a graphitic slit pore of width 3.4 Å because the pore width, as measured by x-ray diffraction coupled with electron diffraction, is the distance between the carbon centers. From simple geometric considerations, it is easy to show that a pore width of $2\sigma_{sf}$ or greater is required to adsorb even a single layer of a fluid inside a slit pore. The solid-fluid interaction diameters is denoted by σ_{sf}. For the hydrogen-graphite system $\sigma_{sf}=3.25$ Å. This means that the platelet spacing must increase dramatically for large amounts of adsorption to take place. The wall spacing is held fixed in the simulations, so we cannot directly compare any single simulation with the nanofiber experiments, because the *in situ* platelet spacing has not been experimentally measured. We should point out in passing that such large expansions of the platelet spacing on hydro-

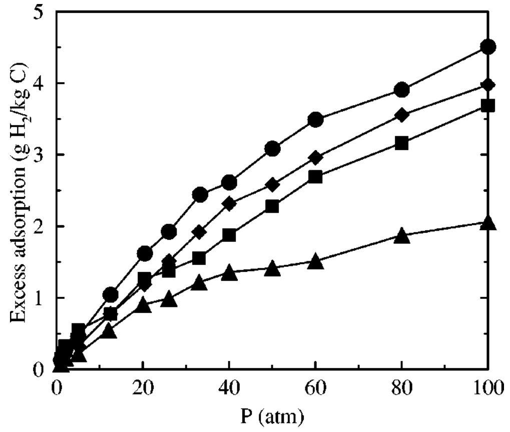

FIG. 4. Excess adsorption isotherms for hydrogen in idealized carbon slit pores of various widths at 298 K. Triangles are for the $H^*=2$ pore, circles are for $H^*=3$, diamonds are for $H^*=4$, and squares are for $H^*=6.67$.

gen up-take should be experimentally observable. We therefore compare each of the four slit pores with the data of Chambers *et al.* The experiments indicate that graphite nanofibers can adsorb on the order of 100–2000 g H_2/kg C at 298 K and an initial pressure of hydrogen of about 100 atm. The highest excess gravimetric density for the slit pores at these conditions is 4.5 g H_2/kg C. This is a factor of 20 less than even the smallest amount of hydrogen adsorption reported by Chambers *et al.* While edge effects are missing from our model, it is difficult to imagine that such large amounts of hydrogen can be adsorbed by the edges of the graphite platelets. Nevertheless, we are currently developing a more sophisticated model of the graphite nanofibers in order to assess the importance of edge effects on adsorption. Figure 4 shows the excess gravimetric adsorption isotherms in various idealized carbon slit pores at 298 K. In contrast to the total adsorption (Fig. 3), the excess adsorption decreases with pore width except for the smallest pore ($H^*=2$). This is due to the fact that the solid-fluid potential in the center of the larger pores is very weak, and therefore has little effect on the gas density near the center of the pore. The density in the center of the largest pore ($H^*=6.7$) is identical to the bulk density. Increasing the pore width to higher values will not increase the excess adsorption in the pore. Therefore, we conclude that any larger separations would not increase the amount of fluid actually adsorbed. From our simulations it appears that the hydrogen uptake reported for graphitic nanofibers cannot be explained in terms of the standard potential models for graphite-hydrogen interactions. It appears that a much stronger and long-ranged solid-fluid interaction potential is needed to explain the very large values of adsorption reported by Chambers *et al.*[9]

B. Adsorption in tube arrays

We have calculated adsorption isotherms for *para*-hydrogen in the (9,9) and (18,18) tube arrays. Adsorption isotherms for the interior of the tube and the interstitial sites were computed from independent GCMC runs. The total adsorption was calculated by simply adding the amounts adsorbed in the tube interior and interstice at each pressure.

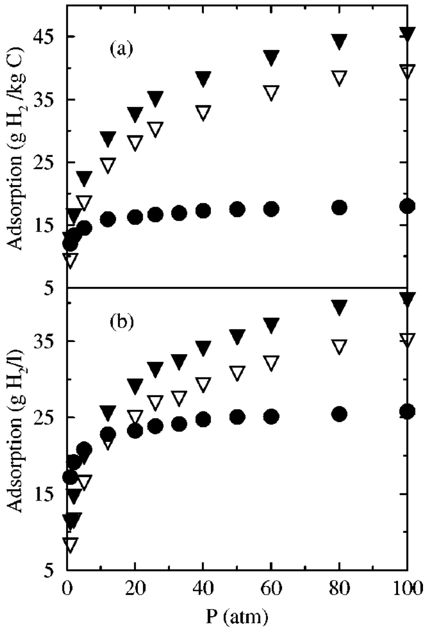

FIG. 5. Adsorption isotherms for hydrogen in SWNT arrays at 77 K. The open circles and triangles represent adsorption inside the (9,9) and (18,18) tubes, respectively. The filled circles and triangles give the total amount adsorbed (including interstitial adsorption) in the (9,9) and (18,18) tube arrays, respectively. The filled circles lie on top of the open circles because there is virtually no interstitial adsorption for the (9,9) tube array.

The adsorption isotherms at 77 K are shown in Fig. 5. The open symbols give the amount of hydrogen adsorbed inside the tube and the filled symbols represent the total amount of adsorption (inside plus interstitial). In the low pressure range, the (9,9) tube array gives higher gravimetric and volumetric densities than the (18,18) tube because of the stronger fluid-wall interaction potential for the (9,9) tube. The gravimetric and volumetric densities in the (18,18) tube array become larger than those in the (9,9) tube at pressures above 5 and 10 atm, respectively. This is due to the larger available volume in the (18,18) tube array. The (9,9) tube has a diameter of 12.2 Å, as measured from the center of the carbon atoms in the tube. It can therefore hold a single layer of hydrogen adsorbed on the inside surface of the tube, plus a single column of hydrogen molecules confined to the center of the tube. The (18,18) tube has a diameter of 24.4 Å and can theoretically hold three concentric rings of hydrogen, and a column of hydrogen in the center of the tube. The volumetric density of the adsorbed hydrogen is based on the total volume of the tube array available for adsorption, including the interstitial space. The total volume of a unit cell containing one tube and two interstices is $\sqrt{3}L(2R+h)^2/2$, where R is the radius of the tube as measured from the carbon centers, and h is the van der Waals gap between the tube walls, also measured from the carbon centers, and L is the length of the tube array. The effective volume is less than the total volume because of steric interactions between the carbon atoms and hydrogen molecules. The ratio of effective volume to total volume is approximately given by

$$\frac{V_{\mathrm{eff}}}{V}=1-\frac{4\pi R\sigma_{sf}}{\sqrt{3}(2R+h)^2}. \tag{7}$$

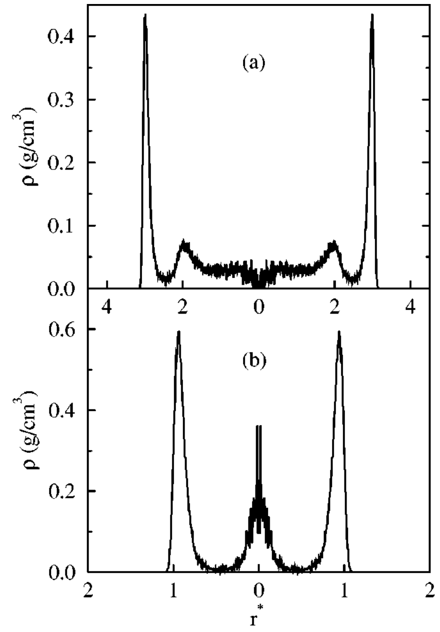

FIG. 6. Density profiles inside the (18,18) and (9,9) tubes at 77 K and 50 atm. The (18,18) tube density is given in (a), and the (9,9) density is shown in (b).

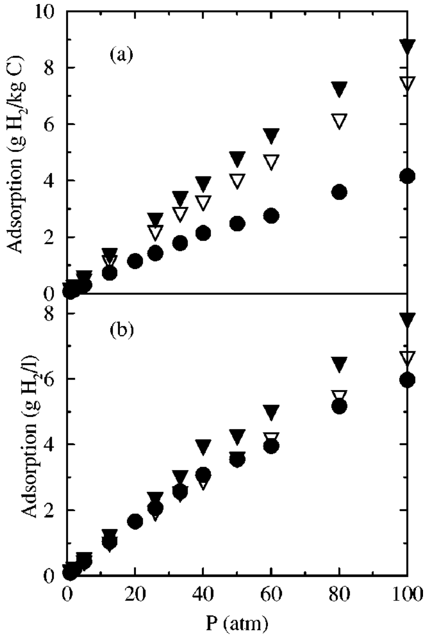

FIG. 7. Adsorption isotherms for hydrogen in SWNT arrays at 298 K. The circles are data for the (9,9) tube arrays, and the triangles are for the (18,18) arrays. As in Fig. 5 the open symbols give the amount adsorbed inside the tubes while the filled symbols give the total adsorption, including the tube interstices. The interstitial adsorption in the (9,9) array is negligible. The gravimetric densities are plotted in (a) and the volumetric densities are plotted in (b).

For the (9,9) tube this ratio turns out to be about 0.4, while for the (18,18) tube it is close to 0.6. This clearly shows why the (18,18) tube array exhibits higher amounts adsorbed at high pressures.

The 77 K adsorption isotherms for the tubes show significant uptake at low pressures. The (9,9) tube becomes essentially saturated at pressures higher than 40 atm where the adsorption isotherm shows a plateau. The solid-fluid potential in the (18,18) tube is fairly weak past the first adsorbed layer, so the fluid density in the center of the (18,18) tube is much lower than for the (9,9) tube at the same pressure. This can be seen from a plot of the density profiles at a pressure of 50 atm as shown in Fig. 6.

Interstitial adsorption constitutes a significant fraction of the total amount adsorbed for the (18,18) tube. However, in the smaller (9,9) interstices, adsorption is negligible because hydrogen is effectively excluded from the interstice due to its large zero-point energy. The (18,18) interstice shows a local enhancement of potential energy analogous to that observed for non-parallel graphitic systems.[43,44] The minimum energy in the interstice is greater than that inside the (18,18) tube by nearly a factor of 2. The (18,18) interstice allows a single row of molecules to adsorb. Interstitial adsorption accounts for at most 14% of the total adsorption for the (18,18) tube array at 77 K.

Quantum effects are significant at 77 K. For example, at 50 atm the density inside the (9,9) tube from classical simulations is about 17% higher than from quantum simulations. Quantum effects are extremely important for calculating interstitial adsorption for the (9,9) tube. The classical simulations for hydrogen adsorption in the (9,9) interstice at 77 K and 50 atm give a value of 0.2 g H_2/kg C. Quantum simulations at the same conditions give 0.004 g H_2/kg C.

Figure 7 shows the gravimetric and volumetric adsorption isotherms in the (9,9) and (18,18) tube arrays at 298 K. Increasing the temperature from 77 to 298 K lowers the amount adsorbed by approximately a factor of 5 at 100 atm. The higher temperature largely masks differences in the adsorption potentials of the two tubes and the amount adsorbed is dominated by the effective volume. The (18,18) tube array adsorbs substantially more hydrogen than the (9,9) tube array over the entire pressure range. Interstitial adsorption constitutes at most 15% of the total amount of adsorption for the (18,18) tube array, but less than 1% for the (9,9) tube. Quantum effects are not as significant at 298 K for adsorption inside the tubes. Calculations for classical hydrogen give about 3% higher adsorption than for quantum hydrogen adsorbing inside the tubes. Surprisingly, quantum effects on adsorption in the interstitial regions are very important at 298 K. Interstitial adsorption from classical simulations is about 40% higher than from quantum simulations for the (9,9) tube. Even for the larger interstice of the (18,18) tube, adsorption of classical hydrogen is 15% higher than for quantum hydrogen. This clearly demonstrates a case where quantum effects are large in a confined system, yet completely absent in the bulk fluid.

The adsorption isotherm data for the (9,9) tube array at 133 K are shown in Fig. 8. The results can be compared with recently reported experimental data for hydrogen adsorption on carbon soots containing 0.1 to 0.2 wt% SWNTs.[4] The diameters of the SWNTs in the soot were estimated to be about 12 Å, which is close to the (9,9) tube diameter of 12.2 Å. The nanotube containing soot was exposed to 300 Torr of hydrogen at 273 K for 10 min, followed by 3 min at 133 K. Temperature programmed desorption was then carried out to

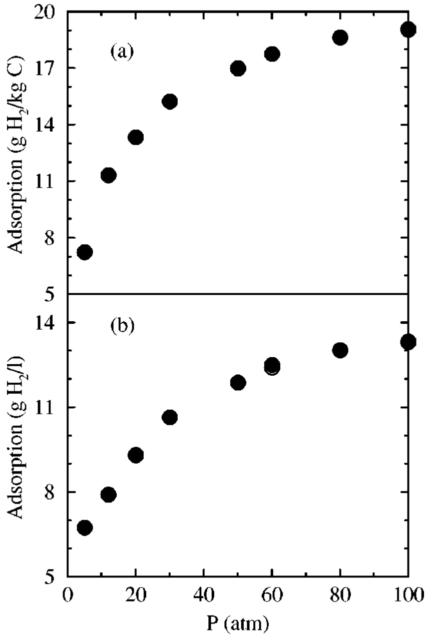

FIG. 8. Adsorption isotherm for hydrogen in an array of (9,9) single-walled nanotubes at 133 K. The gravimetric density is shown in (a) and the volumetric density is shown in (b).

measure the amount of hydrogen adsorbed and the isosteric heat of adsorption. Dillon *et al.* reported an isosteric heat of adsorption of 19.6 kJ mol^{-1}.[4] Simulations at the same conditions yield a value of 6.3 kJ mol^{-1}. Experimental estimates of the amount of hydrogen adsorbed in the nanotubes range from 5 to 10 wt %, while simulation gives 0.8 wt % at 133 K and 300 Torr. Even at the highest pressure studied, 100 atm, the simulation results show only 1.9 wt %, which is still far below the experimental estimate. Much of the discrepancy may be due to inaccuracy in the estimation of the number of nanotubes in the soot. Another potential source of error is our use of a graphite potential to describe the SWNT potential. This potential does not account for the well-known differences in the electronic structure of the tube compared with graphite. We are currently investigating the effect of the solid-fluid potential on the adsorption isotherms of SWNTs. However, there is a need for experiments on high-purity samples of SWNTs in order to facilitate more direct comparison with computer simulations.

C. Comparison of tube and slit pores

Comparing Figs. 2 and 5 we see that the (9,9) and (18,18) tube arrays adsorb less hydrogen on both a volumetric and gravimetric basis than the idealized slit pores of $H^*=3$ and greater. Recall that the $H^*=3$ pore can hold a maximum of two layers of adsorbed hydrogen, one on each surface of the pore walls. The difference between the tubes and the slit pores can be explained in terms of the effective surface area available for adsorption. Most of the external surface area of the tubes is blocked from adsorption by the close-packing of the tube arrays. In addition, the effective surface area inside a tube is only a fraction of the nominal surface area. Given a tube of radius R, the ratio of the effective and nominal surface areas inside the tube is $(R-\sigma_{sf})/R$. The effective surface area ratio for the (9,9) tube is about 0.5, while the ratio for the (18,18) tube is close to 0.7. Even though the solid-fluid potential in the (9,9) tube is more attractive than the $H^*=3$ slit pore, the difference is not enough to make up for the loss of effective surface area.

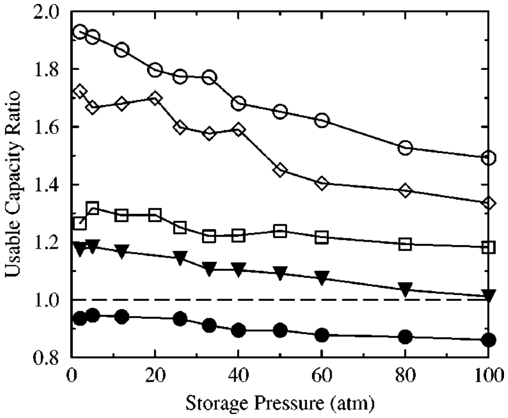

FIG. 9. The usable capacity ratios for SWNT arrays and idealized slit pores at 298 K. The discharge pressure is 1 atm. The filled circles and triangles denote the (9,9) and (18,18) tubes, respectively. The open symbols represent data for the slit pores. Diamonds are for $H^*=2$, circles are for $H^*=3$, and squares are for $H^*=6.67$.

The usable capacity ratio (UCR) is an important criterion used to judge the performance of an adsorbent.[1] The UCR is defined as the mass of available fuel in a sorbent-loaded vessel divided by the mass of available fuel in a vessel without adsorbent (compressed gas only). The available fuel, in this case hydrogen, is the mass of hydrogen in the vessel at the storage, or working pressure, minus the mass of hydrogen in the vessel at the discharge pressure. The UCR is a measure of the effectiveness of physisorption compared to gas compression at the same pressures. If the UCR has a value greater than unity then the sorbent is more effective than compressed gas. If the value is less than unity then physisorption is actually less effective than simple compressed gas storage.

Usable capacity ratios for the (9,9) and (18,18) SWNTs and the idealized graphitic slit pores are plotted as a function of storage pressure in Fig. 9. The discharge pressure is 1 atm and the temperature is 298 K. The slit pores examined in Fig. 9 have widths of $H^*=2$, 3, and 6.67. The value of the UCR for the (9,9) tube is always less than unity for a discharge pressure of one atmosphere. For smaller discharge pressures, the UCR could be greater than unity, but this is not important from a technical view point. Assuming that our solid-fluid interaction potential is accurate, these calculations demonstrate that a close-packed array of (9,9) SWNTs is not an effective sorbent for hydrogen at 298 K. The (18,18) tube has a UCR of about 1.2 at the lowest storage pressure, decreasing to a value just above unity at 100 atm. Note that the UCRs for all sorbents decrease with increasing storage pressure, as expected. All of the slit pores (open symbols in Fig. 9) have UCRs that are larger than the SWNTs. The slit pore of width $H^*=3$ gives the highest UCR, with $H^*=2$ being next highest, and $H^*=6.7$ after that.

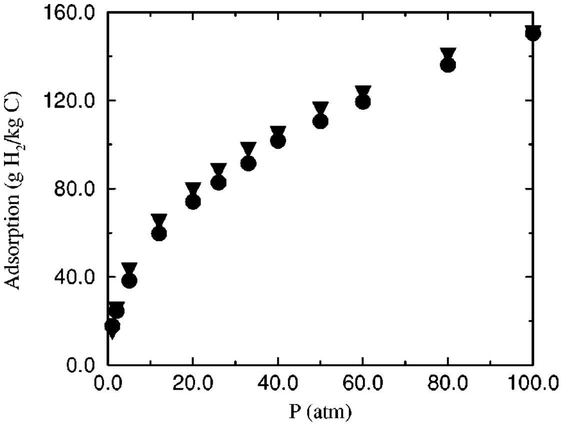

FIG. 10. Adsorption isotherms in isolated SWNTs at 77 K. The circles and triangles denote the total amount adsorbed in the (9,9) and (18,18) tubes, respectively.

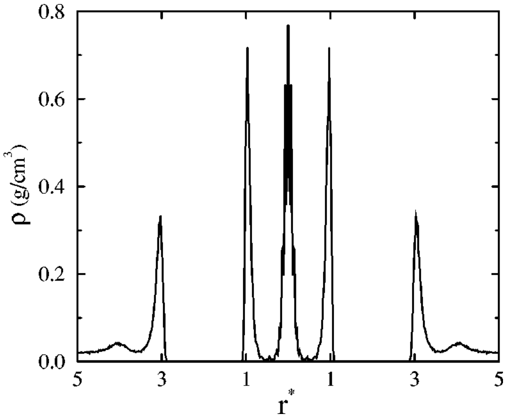

FIG. 11. Density profile for hydrogen adsorbed on the internal and external surface of an isolated SWNT at 77 K and 50 atm.

D. Adsorption in isolated tubes

As noted above, adsorption in the interstices constitutes a small fraction of the total amount adsorbed. Much of the volume and surface area in the tube array is unavailable for adsorption because of steric effects in the close-packed structure of the tubes. The observed van der Waals gap of 3.2 Å is obviously not optimum for hydrogen adsorption. If tubes in the array could be separated from one another, the sorbent would have a greater effective surface area and volume available for adsorption. We have calculated the adsorption of hydrogen on the external and internal surfaces of an isolated SWNT as a test of making the maximum surface area available for adsorption. Figure 10 shows the gravimetric adsorption isotherms of hydrogen for the isolated (9,9) and (18,18) tubes at 77 K. Note that the volumetric density for an isolated tube is not well defined. The solid-fluid potentials used in this case correspond to the isolated tube, not the tube in an array of tubes. The (18,18) tube adsorbs slightly more hydrogen than the (9,9) tube, except at the lowest pressures. The separation of the tubes greatly enhances the gravimetric density of hydrogen over the close-packed tube array at the same conditions. Adsorption on the external surface of the tube makes a significant contribution to the total amount of hydrogen adsorbed. The gravimetric densities in the isolated tubes are comparable to the best idealized slit pore with a width of $H^*=3$ and AX-21 at moderate pressures. At 50 atm the gravimetric density in the (18,18) tube is 70% higher than that in the $H^*=3$ slit pore and 20% higher than for AX-21. Figure 11 shows the density profile of hydrogen adsorbed in the isolated (9,9) tube at 50 atm. The three highest peaks inside the tube correspond to the hydrogen adsorbed on the internal surface of the tube and the column of hydrogen in the center of the tube. Two layers of fluid are adsorbed on the outside surface of the tube, although the second layer is rather low density. The density outside the tube approaches the bulk gas phase density at a distance of about $3\sigma_{ff}$ away from the wall.

V. CONCLUSION

We have calculated the adsorption isotherms of hydrogen in arrays of SWNTs, isolated SWNTs, and idealized carbon slit pores. We have found that the idealized slit pores give significantly better performance for hydrogen storage than SWNT arrays. The gravimetric and volumetric densities in the idealized slit pore with a width of $H^*=3$ operating at 77 K and 50 atm are very close to the DOE targets, although this temperature is much too low to be of use for vehicular fuel storage. The usable capacity ratios for the pore of width $H^*=3$ are substantially higher than those for SWNT arrays. Arrays of SWNTs with a van der Waals gap of 3.2 Å give relatively low usable capacity ratios. This is mainly because of the excluded surface area in the close-packed array of tubes. Hydrogen adsorption in nanotubes is strongly influenced by the effective surface area and volume at high pressures and temperatures. The packing geometry of the SWNTs plays an important role in hydrogen storage. The gravimetric density of hydrogen in isolated tubes at 77 K and 50 atm is well above that for the AX-21 activated carbon and the idealized slit pore of width $H^*=3$. The volumetric density for a tube array can be improved by optimizing the van der Waals gap. Work is in progress on optimizing the packing geometry in tube arrays at different temperatures. None of the adsorbate configurations studied in this work are able to approach the DOE storage goals at ambient temperatures.

These simulations do not confirm the large amounts of hydrogen adsorbed for similar systems of SWNTs and graphitic nanofibers (slit pores) recently observed experimentally.[4,9] While our simulations are only approximations to the real experimental systems, it is difficult to understand the magnitude of hydrogen adsorption reported by Chambers *et al.*[9] in terms of standard statistical mechanical models of adsorption, even considering errors in our adsorption potential.

ACKNOWLEDGMENTS

The authors thank P. Bénard and R. Chahine for helpful discussions and for providing data. Support from the National Science Foundation through a CAREER Grant No. CTS-9702239 to J.K.J. is acknowledged. The donors of The Petroleum Research Fund, administered by the American Chemical Society, and Sandia National Laboratory are acknowledged for partial support of this work.

[1] S. Hynek, W. Fuller, and J. Bentley, Int. J. Hydrogen Energy **22**, 601 (1997).
[2] J. S. Noh, R. K. Agarwal, and J. A. Schwarz, Int. J. Hydrogen Energy **12**, 693 (1987).
[3] K. A. G. Amankwah, J. S. Noh, and J. A. Schwarz, Int. J. Hydrogen Energy **14**, 437 (1989).
[4] A. C. Dillon, K. M. Jones, T. A. Bekkedahl, C. H. Kiang, D. S. Bethune, and M. J. Heben, Nature (London) **386**, 377 (1997).
[5] R. Chahine and T. K. Bose, Int. J. Hydrogen Energy **19**, 161 (1994).
[6] P. Bénard and R. Chahine, Proceedings of the 12th World Hydrogen Energy Conference, 1998, Vol. 2, p. 1121.
[7] P. Bénard and R. Chahine (personal communication).
[8] C. Carpetis and W. Peschka, Int. J. Hydrogen Energy **5**, 539 (1980).
[9] A. Chambers, C. Park, R. T. K. Baker, and N. M. Rodriguez, J. Phys. Chem. **102**, 4253 (1998).
[10] S. Iijima, Nature (London) **354**, 56 (1991).
[11] S. Iijima and T. Ichihashi, Nature (London) **363**, 603 (1993).
[12] D. S. Bethune, C. H. Kiang, M. S. de Vries, G. Gorman, R. Savoy, J. Vazquez, and R. Beyers, Nature (London) **363**, 605 (1993).
[13] S. Amelinckx, X. B. Zhang, D. Bernaerts, X. F. Zhang, V. Ivanov, and J. B. Nagy, Science **265**, 635 (1994).
[14] A. Thess *et al.*, Science **273**, 483 (1996).
[15] T. W. Ebbesen, *Carbon Nanotubes, Preparation and Properties* (CRC, Boca Raton, FL, 1997).
[16] J. E. Fischer, H. Dai, A. Thess, R. Lee, N. M. Hanjani, D. L. Dehaas, and R. E. Smalley, Phys. Rev. B **55**, R4921 (1997).
[17] S. C. Tang, P. J. F. Harris, and M. L. H. Green, Nature (London) **363**, 520 (1993).
[18] P. M. Ajayan, T. W. Ebbesen, J. Ichihashi, S. Iijima, K. Tanigaki, and H. Hiura, Nature (London) **363**, 522 (1993).
[19] M. R. Pederson and J. Q. Broughton, Phys. Rev. Lett. **69**, 2689 (1992).
[20] K. F. Schmidt, Sci. News **143**, 279 (1993).
[21] P. M. Ajayan and S. Iijima, Nature (London) **361**, 333 (1993).
[22] J. Sloan, J. Hammer, M. Zwiefka-Sibley, and M. L. H. Green, Chem. Commun. (Cambridge) **1998**, 347 (1998).
[23] M. W. Maddox and K. E. Gubbins, Langmuir **11**, 3988 (1995).
[24] G. Stan and M. W. Cole, J. Low Temp. Phys. **110**, 539 (1998).
[25] K. R. Matranga, A. L. Myers, and E. D. Glandt, Chem. Eng. Sci. **47**, 1569 (1992).
[26] R. F. Cracknell, P. Gordon, and K. E. Gubbins, J. Phys. Chem. **97**, 494 (1993).
[27] Q. Wang, J. K. Johnson, and J. Q. Broughton, Mol. Phys. **89**, 1105 (1996).
[28] Q. Wang and J. K. Johnson, Fluid Phase Equilibria **132**, 93 (1997).
[29] Q. Wang, J. K. Johnson, and J. Q. Broughton, J. Chem. Phys. **107**, 5108 (1997).
[30] Q. Wang and J. K. Johnson, Mol. Phys. **95**, 299 (1998).
[31] I. F. Silvera and V. V. Goldman, J. Chem. Phys. **69**, 4209 (1978).
[32] A. D. Crowell and J. S. Brown, Surf. Sci. **123**, 296 (1982).
[33] J. W. Mintmire, B. I. Dunlap, and C. T. White, Phys. Rev. Lett. **68**, 631 (1992).
[34] N. Hamada, S. Sawada, and A. Oshiyama, Phys. Rev. Lett. **68**, 1579 (1992).
[35] R. Saito, M. Fujita, G. Dresselhaus, and M. S. Dresselhaus, Appl. Phys. Lett. **60**, 2204 (1992).
[36] G. J. Tjatjopoulos, D. L. Feke, and J. A. Mann, Jr., J. Phys. Chem. **92**, 4006 (1988).
[37] W. H. Press, B. P. Flannery, S. A. Teukolsky, and W. T. Vetterling, *Numerical Recipes* (Cambridge University Press, Cambridge, 1987).
[38] R. P. Feynman, Rev. Mod. Phys. **20**, 367 (1948); R. P. Feynman and A. R. Hibbs, *Quantum Mechanics and Path Integrals* (McGraw–Hill, New York, 1965).
[39] M. E. Tukerman, B. J. Berne, G. J. Martyna, and M. L. Klein, J. Chem. Phys. **99**, 2796 (1993).
[40] A. L. Pereira, F. A. B. Chaves, and E. Lerner, J. Low Temp. Phys. **88**, 421 (1992).
[41] J. G. Daunt, S. G. Hedge, S. P. Tsui, and E. Lerner, J. Low Temp. Phys. **44**, 207 (1981).
[42] F. C. Motteler and J. G. Dash, Phys. Rev. B **31**, 346 (1985).
[43] M. J. Bojan, R. van Slooten, and W. Steele, Sep. Sci. Technol. **27**, 1837 (1992).
[44] M. J. Bojan, E. Cheng, M. W. Cole, and W. Steele, Adsorption **2**, 53 (1996).